PCCP

ROYAL SOCIETY OF CHEMISTRY

PAPER

View Article Online
View Journal | View Issue

Check for updates

Cite this: *Phys. Chem. Chem. Phys.*, 2025, **27**, 17245

Revisiting the bonding nature of pyramidane: an analogue of the CO molecule†

Qinqin Yuan,‡[a] Zhiruo Ding,‡[a] Dan Li*[a] and Longjiu Cheng *[ab]

Received 6th June 2025,
Accepted 17th July 2025

DOI: 10.1039/d5cp02142a

rsc.li/pccp

Pyramidane ($C(C_4H_4)$) and its derivatives have garnered considerable interest in organic and synthetic chemistry due to their distinctive pyramidal geometry. Nevertheless, the non-classical bonding pattern between the pyramidal apex and base remains insufficiently elucidated. This work firstly developed a two-dimensional (2D) superatom–atom super bonding framework, providing new insights into the bonding nature of $C(C_4H_4)$. Specifically, the π-conjugated C_4H_4 unit acts as a 2D $^{\diamond}$O superatom with four π-electrons, enabling interaction with the apical carbon atom to form a CO-type superatomic molecule *via* a super triple bond, satisfying the electron closed shell for both $^{\diamond}$O and C. Subsequently, a series of coordination complexes, $Pd[C(C_4H_4)]_n$ (n = 1–4), are designed to further explore the chemical bonding abilities, wherein each $C(C_4H_4)$ interacts with the Pd center *via* a σ bond and several multicenter d–π* bonds. Moreover, we design two stable 2D all-carbon monolayers derived from pyramidane-based assemblies, which exhibit good stability, feasible synthetic accessibility, and moderate band gaps under certain strain conditions, suggesting potential electronic applications. This work revisits the bonding paradigm of $C(C_4H_4)$ and broadens our understanding of chemical interactions, offering a new strategy for the design of clusters and materials *via* 2D superatom–atom bonding.

Published on 18 Adooleessa 2025. Downloaded on 16/10/2025 3:00:56 PM.

1. Introduction

Pyramidane and its derivatives have long focal targets in synthetic chemistry, captivating organic chemists for over five decades due to their mesmerizing geometric structures.[1–6] A thorough understanding of their electronic structures can provide valuable insights into non-classical bonding paradigms and facilitate the rational design of novel materials with tailored electronic properties. To date, several substituted tetrahedranes, incorporating isoelectronic main-group elements at specific vertices, have been successfully synthesized and characterized.[2–4] However, the parent pyramidane as the simplest organic system comprising a C_4 base and a pyramidal carbon apex has yet to be experimentally observed. Although theoretical studies have established that $C(C_4H_4)$ represents a stable minimum on the potential energy surface and features covalent interactions between its carbon apex and C_4H_4 base,[6–10] only limited analysis of canonical molecular orbitals (MOs) and the Wade–Mingos–Rudolph rule have been used to elucidate the covalent nature of the non-classical apex-to-base interactions involving six delocalized electrons. Further detailed insights into the molecular bonding in $C(C_4H_4)$ would be valuable for advancing the understanding of related systems and for guiding the design of $C(C_4H_4)$-based materials.

Based on the Jellium model and the super valence bond theory originally developed for metal clusters,[11–17] our group recently proposed a two-dimensional (2D) superatomic-molecule theory to establish a generalized electron counting rule for π-conjugated systems.[18] Within this framework, conjugated units of varying ring sizes are treated as 2D superatoms following the revised Jellium model ($|1S^2|1P^4|1D^4|\ldots$). Specifically, conjugated units containing 2, 6 and 10 π-electrons are designated as closed-shell 2D analogues of He, Ne and Ar, respectively, and are termed close–shell $^{\diamond}$He, $^{\diamond}$Ne, and $^{\diamond}$Ar superatoms. In contrast, conjugated units with 9, 8, 7, 5, 4, 3, and 1 π-electrons are classified as open-shell $^{\diamond}$P, $^{\diamond}$S, $^{\diamond}$Cl, $^{\diamond}$F, $^{\diamond}$O, $^{\diamond}$N and $^{\diamond}$H superatoms, which can further form superatomic bonds with adjacent units to achieve π-electron closed-shell configurations, analogous to the behavior of traditional

[a] *Department of Chemistry, Anhui University, Hefei, Anhui 230601, P. R. China. E-mail: ahulidan@aliyun.com, clj@ustc.edu*
[b] *Key Laboratory of Functional Inorganic Materials of Anhui Province, Anhui University, Hefei, Anhui 230601, P. R. China*

† Electronic supplementary information (ESI) available: ELF maps of (a) $C(C_4H_4)$ and (b) CO on the *x*–*y* planes (Fig. S1); the optimized structure and the energy (E_{H-L}) gap between the highest occupied molecular orbital (HOMO) and the lowest unoccupied molecular orbital (LUMO) for $Ni[C(C_4H_4)]_4$, $Pt[C(C_4H_4)]_4$, $Fe(CO)_5$, $Fe(CO)_4[C(C_4H_4)]$, and $Fe(CO)_3[C(C_4H_4)]_2$ (Fig. S2). AIMD simulations at 300 and 500 K for the (a) **C_5-A** and (b) **C_5-B** monolayers (Fig. S3); Young's modulus and Poisson's ratio for the (a) **C_5-A** and (b) **C_5-B** monolayers (Fig. S4); binding energy (E_b) and the HOMO–LUMO gap (E_{H-L}) of C_4H_4-M (M = C, Si, Ge, and Sn) (Table S1); optimized Cartesian coordinates (in angstroms) of the unit cell for CO, $C(C_4H_4)$, $Pd(CO)_{1-4}$, $Pd[C(C_4H_4)]_{1-4}$, **C_5-A** and **C_5-B** monolayers (Table S2). See DOI: https://doi.org/10.1039/d5cp02142a

‡ These authors contributed equally to this work.

Published on 18 Adooleessa 2025. Downloaded on 16/10/2025 3:00:56 PM.

atoms.[19–23] Given the successful extension of the super valence bond model to describe the superatom–atom super bonding in $Au_{16}X_4$ (X = F, Cl or Br) metallic clusters[24] and the $(B_3CB_3)N_2$ monolayer,[25] we infer whether the C_4H_4 base in $C(C_4H_4)$ can act as a 2D $^{\diamond}O$ superatom with four conjugated π-electrons, enabling bonding to the apical carbon atom *via* a 2D superatom–atom super interaction, reminiscent of the bonding in CO molecules.

In this work, we combine the 2D superatomic-molecule theory with the superatom–atom super bonding model to elucidate the electronic structure of $C(C_4H_4)$, wherein the π-conjugated C_4H_4 unit indeed functions as a 2D $^{\diamond}O$ superatom and forms a super triple bond with the apical carbon atom, as evidenced by chemical bonding analysis. Furthermore, we design a series of coordination complexes, $Pd[C(C_4H_4)]_n$ (n = 1 to 4), along with two stable $C(C_4H_4)$-based 2D all-carbon monolayers exhibiting moderate band gaps, to explore the potential applications of this bonding framework. These findings offer new perspectives on the bonding nature of $C(C_4H_4)$ and underscore the broader significance of 2D superatom-atom bonding in cluster chemistry and material design.

2. Computational details

Geometry optimization and vibrational frequency calculations for $C(C_4H_4)$, CO, and their corresponding metal complexes were performed using Gaussian 16[26] at the PBE0/def2-TZVP[27,28] level of theory. Binding energy was determined using the BP86/def2-TZVP protocol.[29–31] Electronic structure analyses, including adaptive natural density partitioning (AdNDP)[32] and electron localization function (ELF)[33] studies, were systematically conducted using the Multiwfn software,[34] while molecular orbitals and bonding patterns were visualized using VMD.[35]

First principles calculations for periodic materials were carried out using the Vienna *ab initio* simulation package (VASP)[36–39] using the projected-augmented wave (PAW) method.[40] The exchange–correlation functional was treated within the generalized gradient approximation (GGA)[41] using the Perdew–Burke–Ernzerhof (PBE)[42] functional. A plane wave energy cutoff of 560 eV and a 10 × 10 × 1 Monkhorst–Pack[43] *k*-grid for Brillouin zone sampling were used for the geometry calculations. Force and energy convergence accuracy were set to 0.02 eV $Å^{-1}$ and 10^{-6} eV, respectively. A 15 Å vacuum layer was introduced along the *z*-direction to eliminate interlayer interactions. The electronic band structures were determined using the Heyd–Scuseria–Ernzerhof (HSE06)[44] hybrid functional, yielding results consistent with previous experimental data. Phonon dispersion curves were obtained *via* density functional perturbation theory (DFPT)[45] using the Phonopy package.[46] *Ab initio* molecular dynamics (AIMD) simulations were performed in the NVT ensemble with a 4 × 4 × 1 supercell and temperature control *via* a Nosé–Hoover[47] thermostat. The system was equilibrated for 5.0 ps with a 1.0 fs timestep. Chemical bonding in the C_5 monolayers was analyzed using the solid-state adaptive natural density partitioning (SSAdNDP)[48] method with the def2-TZVP basis set applied to the plane wave projection of the electron density matrix. All the monolayer structures were visualized using the VESTA software.[49]

3. Results and discussion

3.1. Geometric structure of $C(C_4H_4)$

As depicted in Fig. 1, the PBE0/def2-TZVP optimized structure of $C(C_4H_4)$ adopts a pyramidal configuration with C_{4v} symmetry and features a substantial energy gap of 8.14 eV between its highest occupied molecular orbital (HOMO) and lowest unoccupied molecular orbital (LUMO). The apical carbon atom exhibits a bond length of 1.63 Å with the planar carbons, slightly exceeding the typical C–C single bond length (1.54 Å), while the four equivalent C–C bonds within the C_4H_4 base measure 1.44 Å, falling between the standard C–C single (1.54 Å) and C=C double (1.34 Å) bond lengths. These observations suggest a unique interaction between the apical carbon and the C_4H_4 base.

3.2. Bonding analysis of $C(C_4H_4)$

As previously reported, each basal C atom bonds to one H and two adjacent C atoms, leaving the residual p orbital electrons of

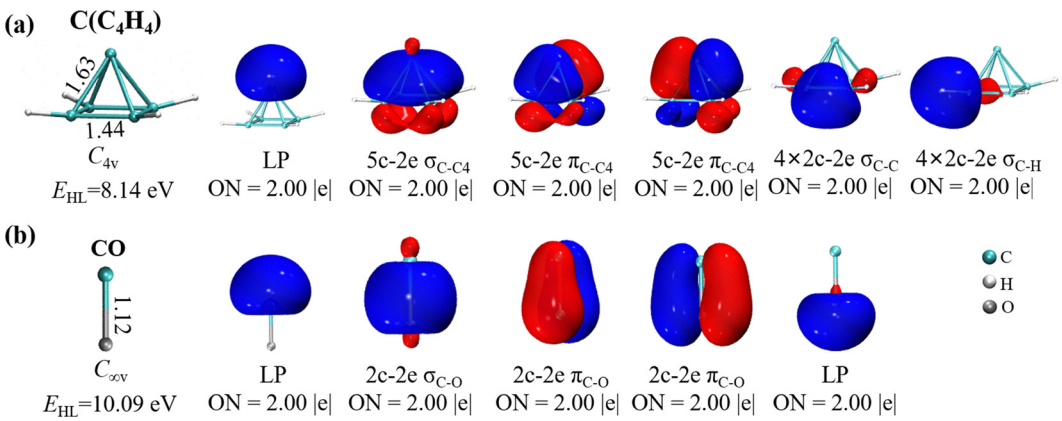

Fig. 1 PBE0/def2-TZVP optimized structures with key bond lengths, AdNDP localized bonds, and electronic occupation numbers (ONs) of the (a) $C(C_4H_4)$ and (b) CO molecules. The carbon, hydrogen and oxygen atoms are represented by cyan, white and grey balls, respectively.

 This journal is © the Owner Societies 2025

Published on 18 Adooleessa 2025. Downloaded on 16/10/2025 3:00:56 PM.

the C_4H_4 base and the relative orbitals of the apical carbon available to form a delocalized π bond.[4,6] Based on the 2D superatomic-molecule theory,[18] the C_4H_4 unit acts as a 2D $^{\diamond}O$ superatom (S^2P^2) possessing four π-electrons, which bonds with the apical carbon to yield a CO-type superatomic molecule comprising two double bonds and one coordination bond to satisfy the superatomic sextet rule for $^{\diamond}O$ and the octet rule for C. To validate this 2D superatom-to-atom bonding model and yield chemically intuitive bonding pictures, AdNDP analysis comparing the bonding patterns of $C(C_4H_4)$ and CO is shown in Fig. 1. The apical carbon possesses a lone pair (LP) with an occupancy number (ON) of 2.00 |e|, whereas each basal carbon participates in a two-center-two-electron (2c–2e) bond (ON = 2.00 |e|) with its neighboring C and H atoms. Furthermore, three 5c–2e bonds (ON = 2.00 |e|) interconnect the carbon apex and the π-conjugated C_4H_4 base. careful examination reveals that the bonding orbitals of $C(C_4H_4)$ exhibit a similar pattern to those in the CO molecule.

This bonding resemblance is further verified by comparing the orbital interactions between the apical carbon and the C_4H_4 base to those in free CO (Fig. 2). Notably, only the conjugated p-orbitals in C_4H_4, namely, the super orbitals of the 2D $^{\diamond}O$ superatom, are considered to explore the interaction between C and C_4H_4. The result indicates that the HOMO of $C(C_4H_4)$ combines the s and p_z orbitals of the apical carbon with the super-S orbital of the C_4H_4 base, while the degenerate HOMO−1 and HOMO−2 orbitals correspond to π bonding MOs formed by the interaction of the apical carbon p orbitals with the super-P orbitals of C_4H_4. These orbital interactions mirror those in CO, supporting the superatomic bonding pattern in $C(C_4H_4)$. This finding is reinforced by electronic localization function (ELF) analysis (Fig. S1, ESI†), which highlights five-center bonds in $C(C_4H_4)$ and two-center bonds in CO *via* conspicuous yellow–green isosurfaces. Furthermore, the calculated Wiberg bond indexes of 3.95 for $C(C_4H_4)$ and 3.37 for CO reconfirm the triple bond character. Collectively, the non-classical apex-to-base interactions in $C(C_4H_4)$ represent a super triple bond mediated by six delocalized electrons, closely paralleling the bonding pattern in CO.

3.3. Coordination abilities of $C(C_4H_4)$

Considering the analogous bonding patterns between the $C(C_4H_4)$ and CO molecules, it is compelling to investigate the coordination ability of $C(C_4H_4)$. For this purpose, we design a series of $Pd[C(C_4H_4)]_n$ (n = 1–4) clusters. As presented in Fig. 3, the Pd center in $PdC(C_4H_4)$ retains three LPs (d_{z^2}, $d_{x^2-y^2}$, and d_{xy}). One coordination σ bond is formed by the LP of the apical carbon to the Pd s orbital, while two feedback π-bonding orbitals arise from the Pd d_{yz} and d_{zx} orbitals coupling with the empty π* orbitals of the super CO entity. All these LPs and bonds present ONs approximately equaling 2.00 |e|. $Pd[C(C_4H_4)]_2$ contains two coordination σ bonds, two feedback π bonds and three LPs, consistent with the spatial distribution of the Pd d orbitals. For $Pd[C(C_4H_4)]_3$ and $Pd[C(C_4H_4)]_4$, four and five feedback π bonds, respectively, are identified. The AdNDP analysis of $Pd(CO)_n$ (n = 1–4) clusters, illustrated in Fig. 3, reveals bonding orbital characteristics similar to those of $Pd[C(C_4H_4)]_n$ (n = 1–4), thereby validating the treatment of the $C(C_4H_4)$ unit as an electronic analogue of CO that interacts with Pd *via* a σ and several multicenter d-π* bonds. Moreover, the structures and their E_{H-L} for $Ni[C(C_4H_4)]_4$, $Pt[C(C_4H_4)]_4$, $Fe(CO)_5$, $Fe(CO)_4[C(C_4H_4)]$, and $Fe(CO)_3[C(C_4H_4)]_2$ further demonstrate the similarity of the bonding nature between CO and $C(C_4H_4)$.

Table 1 quantitatively compares the Pd–C bond lengths, bond orders, HOMO–LUMO gaps, and binding energies of the $Pd(CO)_n$ and $Pd[C(C_4H_4)]_n$ (n = 1–4) clusters. Notably, $Pd[C(C_4H_4)]_n$ exhibits longer Pd–C distances and lower bond

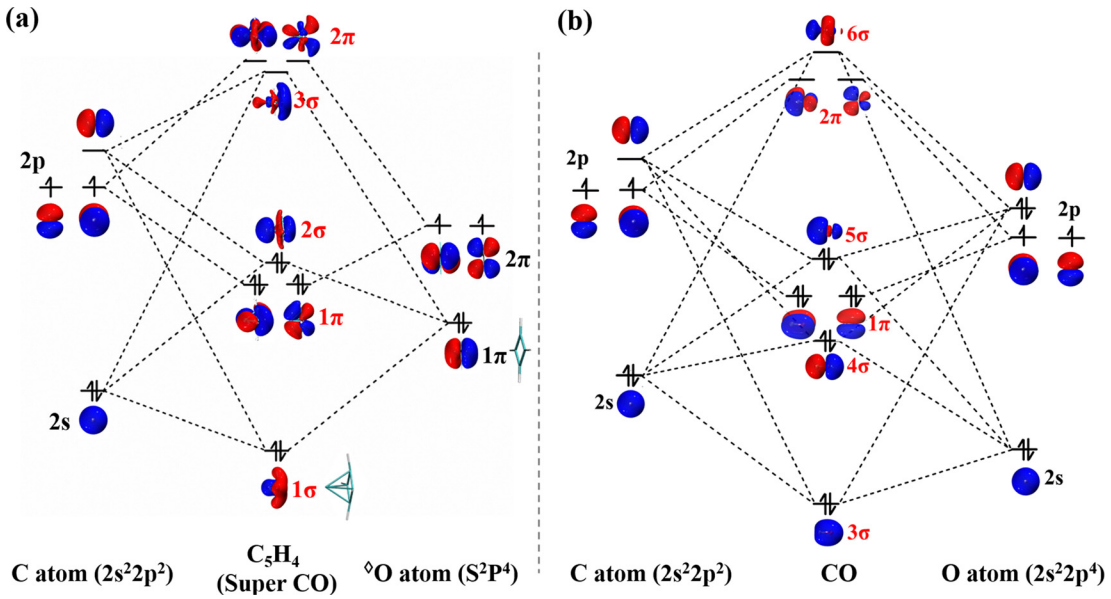

Fig. 2 Scheme of orbital interactions visualizing the molecular orbital formation for (a) $C(C_4H_4)$ and (b) CO molecules.

Published on 18 Adooleessa 2025. Downloaded on 16/10/2025 3:00:56 PM.

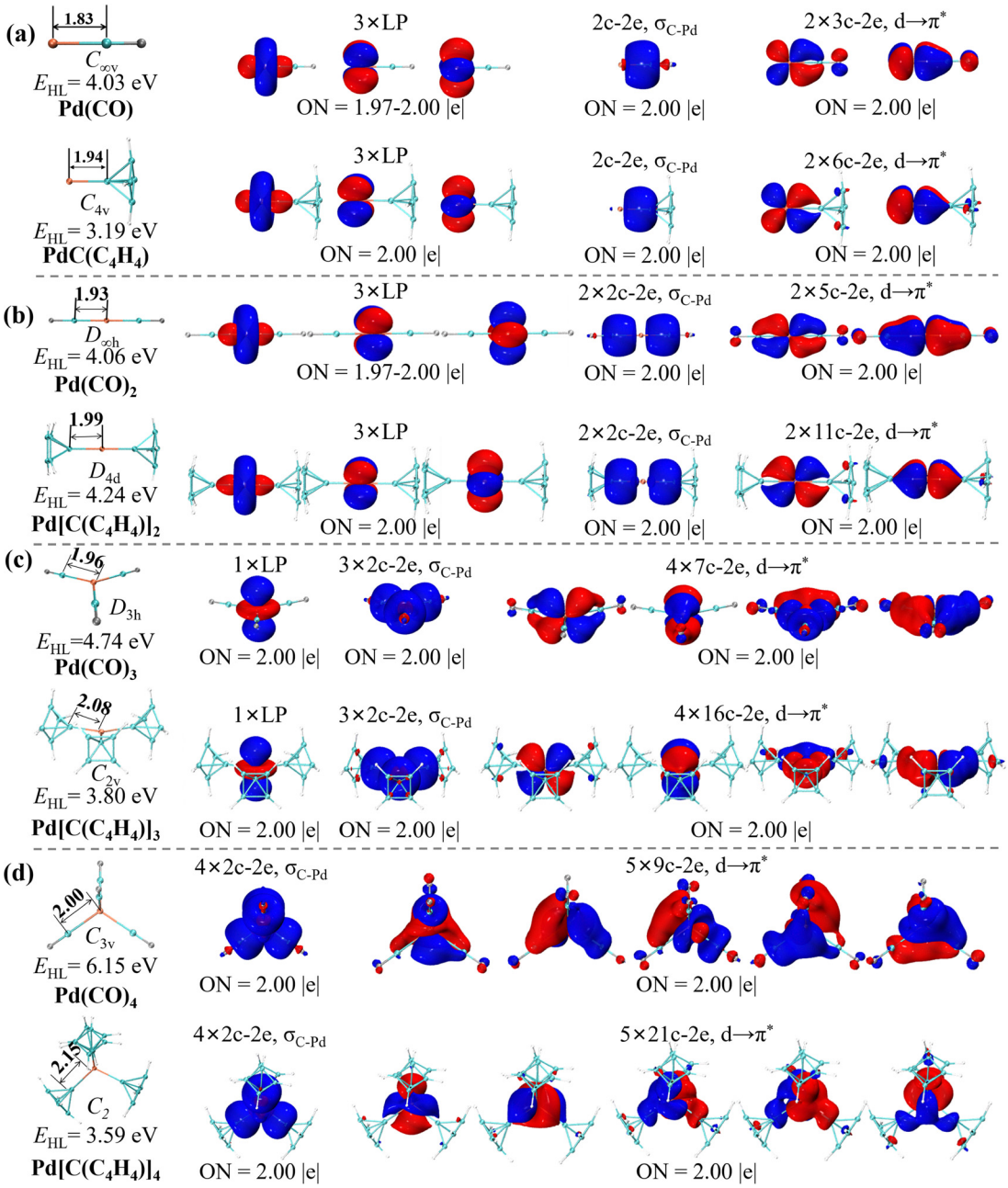

Fig. 3 AdNDP localized bonds and electronic occupation numbers (ONs) of (a) Pd(CO) and PdC(C_4H_4), (b) Pd(CO)$_2$ and Pd[C(C_4H_4)]$_2$, (c) Pd(CO)$_3$ and Pd[C(C_4H_4)]$_3$, as well as (d) Pd(CO)$_4$ and Pd[C(C_4H_4)]$_4$. Notably, the bonding orbitals of the C–C and C–H bonds within the C(C_4H_4) unit are not listed.

orders than their Pd(CO)$_n$ counterparts, indicating relatively weaker coordination interactions in the former. Analysis of the HOMO–LUMO energy gaps and binding energies reveals a non-monotonic stability trend for the Pd[C(C_4H_4)]$_n$ clusters: Pd[C(C_4H_4)] (3.19 eV/−191.71 kJ mol^{-1}) < Pd[C(C_4H_4)]$_2$ (4.24 eV/−358.73 kJ mol^{-1}) > Pd[C(C_4H_4)]$_3$ (3.80 eV/−330.82 kJ mol^{-1}) > Pd[C(C_4H_4)]$_4$ (3.59 eV/−303.67 kJ mol^{-1}), contrasting with the monotonic stabilization enhancement observed with increasing number n in the Pd(CO)$_n$ series. This deviation stems from significant steric hindrance among the C(C_4H_4) ligands and a concomitant reduction in the Pd–C orbital overlap. Moreover, the binding energies in Table S1 (ESI) further demonstrate that substituting the apical carbon atom with Si, Ge and Sn atoms diminishes binding energies, underscoring the superior suitability of carbon for building stable pyramidal structures.

3.4. Structure and stability of the C(C_4H_4)-based C_5-A and C_5-B monolayers

2D materials are widely recognized for achieving superior photocatalytic efficiency relative to bulk materials.[50,51] From a structural design standpoint, the C(C_4H_4) molecule

 This journal is © the Owner Societies 2025

Published on 18 Adooleessa 2025. Downloaded on 16/10/2025 3:00:56 PM.

Table 1 Symmetries, Pd–C bond lengths (R_{Pd-C}, in Å) and bond orders, HOMO–LUMO energy gaps (E_{H-L}, in eV), and binding energies (E_b, in kJ mol^{-1}) of the Pd(CO)$_n$ and Pd[C(C$_4$H$_4$)]$_n$ (n = 1–4) clusters

Molecule	Symmetry	R_{Pd-C}	Bond order	E_{H-L}	E_b
Pd(CO)	$C_{\infty v}$	1.83	1.55	4.03	−237.48
Pd(CO)$_2$	$D_{\infty h}$	1.93	1.22	4.06	−395.97
Pd(CO)$_3$	D_{3h}	1.96	1.16	4.74	−479.86
Pd(CO)$_4$	C_{3v}	2.00	1.09	6.15	−528.56
PdC(C$_4$H$_4$)	C_{4v}	1.94	1.10	3.19	−191.71
Pd[C(C$_4$H$_4$)]$_2$	D_{4d}	1.99	0.95	4.24	−358.73
Pd[C(C$_4$H$_4$)]$_3$	C_{2v}	2.08	0.85	3.80	−330.82
Pd[C(C$_4$H$_4$)]$_4$	C_2	2.15	0.78	3.59	−303.67

demonstrates significant potential for extension into 2D planar architectures *via* controlled polymerization, potentially leading to enhanced material properties with critical implications for guiding the rational design of advanced 2D systems. As illustrated in Fig. 4a and b, removal of all hydrogen atoms from C(C$_4$H$_4$) followed by connection of each basal carbon to an adjacent pyramidal dehydrogenated C(C$_4$H$_4$) unit yields two distinct all-carbon monolayers, denoted as the **C$_5$-A** and **C$_5$-B** monolayers. In **C$_5$-A**, the pyramid units alternate in an up-and-down arrangement, whereas **C$_5$-B** features uniformly aligned pyramids. The **C$_5$-A** and **C$_5$-B** monolayers consist of unit cells containing five and ten carbon atoms, respectively, with lattice parameters of $a = b = 4.93$ (**C$_5$-A**) and $a = b = 3.51$ Å (**C$_5$-B**). Both monolayers share the identical interaxial angles of $\alpha = \beta = \gamma = 90^\circ$ and comparable thicknesses (1.30 for **C$_5$-A** and 1.35 Å for **C$_5$-B**). The intra-pyramid C–C bond lengths measure 1.68/1.46 Å in **C$_5$-A** and 1.70/1.46 Å in **C$_5$-B**, closely aligning with those in isolated C(C$_4$H$_4$) (1.63/1.44 Å), suggesting a similar bonding nature. The inter-pyramidal C–C bonds measure 1.43 (**C$_5$-A**) and 1.44 Å (**C$_5$-B**). The relatively shorter C–C bonds in **C$_5$-A** relative to those in **C$_5$-B** suggest greater stability for the former.

While both monolayers exhibit favorable structural stability based on the optimized molecular geometries, systematic stability evaluations from dynamical, thermal, and mechanical perspectives are essential to assess their practical applicability. We therefore performed a comprehensive theoretical study encompassing stability assessment and experimental synthesis feasibility predictions. The absence of imaginary frequencies in the phonon dispersion spectra (Fig. 4c and d) throughout the whole Brillouin zone confirms their dynamical stability. AIMD simulations at 300, 500 and 1000 K over 5 ps (Fig. 4e, f, and Fig. S2, ESI†) present negligible energy fluctuations and structural distortions, validating robust thermal stability up to 1000 K.

Mechanical stability was evaluated using the elastic constants (C_{ij}), Young's modulus (Y), and Poisson's ratio (ν) (Table 2). All eigenvalues of the elastic constant matrix are positive and meet the Born criteria[52] for 2D materials ($C_{11}C_{22}-C_{12}^2 > 0$ and $C_{66} > 0$), indicative of good mechanical stability. The orientation-dependent Young's modulus and Poisson's ratio, derived as functions of the in-plane θ, are plotted in Fig. S4 (ESI†), demonstrating anisotropic behavior. The magnitudes of $Y(\theta)$ range from 137.54 to 293.52 N m^{-1} for **C$_5$-A** and from 130.03 to 290.40 N m^{-1} for **C$_5$-B**, intermediate between those of graphene (342 N m^{-1})[53] and MoS_2 (123 N m^{-1}).[54] Additionally, $\nu(\theta)$, which quantifies the transverse synthetic strain of materials under the corresponding axial loading, varies between 0.109–0.582 (**C$_5$-A**) and 0.100–0.597 N m^{-1} (**C$_5$-B**). These results suggest strong in-plane flexibility and deformation resistance, positioning both monolayers as promising candidates for strain-engineered band structure modulation.

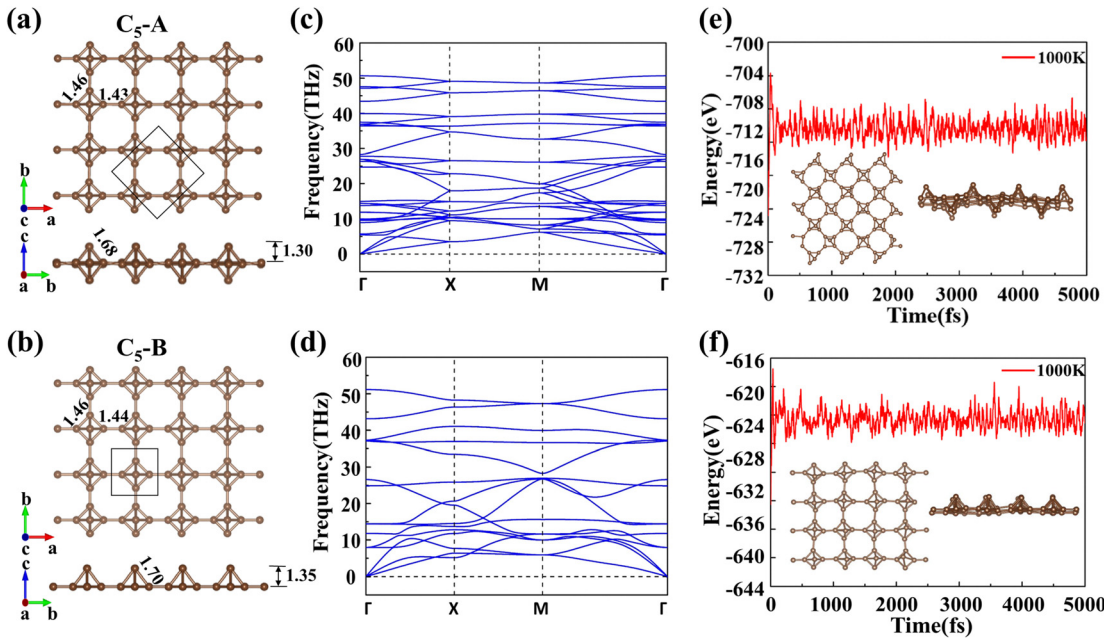

Fig. 4 Top and side views of the optimized geometric structures of the (a) **C$_5$-A** and (b) **C$_5$-B** monolayers. Phonon dispersion curves of (c) **C$_5$-A** and (d) **C$_5$-B**. AIMD simulations at 1000 K showing energy fluctuations with time step and its snapshot of (e) **C$_5$-A** and (f) **C$_5$-B**. The golden balls represent carbon atoms.

Published on 18 Adooleessa 2025. Downloaded on 16/10/2025 3:00:56 PM.

Table 2 Elastic constants (C_{ij}, N m^{-1}), Young's modulus (Y, N m^{-1}), and Poisson's ratio (v, N m^{-1}) of the C_5-A and C_5-B monolayers

	$C_{11} = C_{22}$	$C_{12} = C_{21}$	C_{66}	Y_{2D}	v
C5-A	208.156	121.238	132.344	137.54–293.52	0.109–0.582
C5-B	293.305	29.184	40.719	130.03–290.40	0.100–0.597

Experimental synthesis feasibility was characterized by cohesive energy (E_{coh}) defined as $E_{coh} = (E_{total} - nE_C)/n$, where E_{total} and E_C represent the total energies of the unit cell and the energy of a single C atom, respectively, and n is the number of C atoms per unit cell. The calculated E_{coh} values of −7.96 eV per atom for **C_5-A** and −7.92 eV per atom for **C_5-B** are slightly larger than the theoretical values of graphene (−9.23 eV per atom)[55] and penta-graphene (−8.35 eV per atom),[56] yet match that of experimentally synthesized T-carbon (−7.92 eV per atom)[57] at the same theoretical level, indicating experimental synthesis viability for both monolayers.

3.5. Electronic properties of C_5-A and C_5-B monolayers

The electronic properties of the materials are intrinsically linked to the possible applications. The electronic characteristics of both monolayers were explored *via* the electron band structure and partial density of states (PDOS), as illustrated in Fig. 5a and b. The **C_5-A** monolayer exhibits indirect bandgaps of 2.05 (PBE) and 2.90 eV (HSE06), with the valence band maximum (VBM) and the conduction band minimum (CBM) located at the X and Γ points, respectively. In contrast, the **C_5-B** monolayer manifests direct bandgaps of 1.87 (PBE) and 2.70 eV (HSE06), with both the VBM and the CBM situated at the Γ point. HSE06-based PDOS analysis shows that the CBM is primarily derived from carbon p orbitals, while the VBM arises from s–p hybridization. Given that strain manipulation is an effective strategy for tuning the electronic properties of the CBM and the VBM, a biaxial strain ranging from −3% to 3% was applied to both monolayers to examine the evolution of VBM and CBM energy levels at the HSE06 level (Fig. 5c and d). Increasing tensile strain reduces both the VBM and CBM energies, with a more pronounced decline in the VBM than in the CBM, resulting in a tensile-induced bandgap blueshift for both monolayers.

3.6. Chemical bonding analysis of C_5-A and C_5-B monolayers

To decode the bonding characteristics and stabilization mechanisms of both monolayers, SSAdNDP analysis was performed to visualize electron arrangements *via* chemically intuitive bonding representations (Fig. 6a and b). Similar to $C(C_4H_4)$,

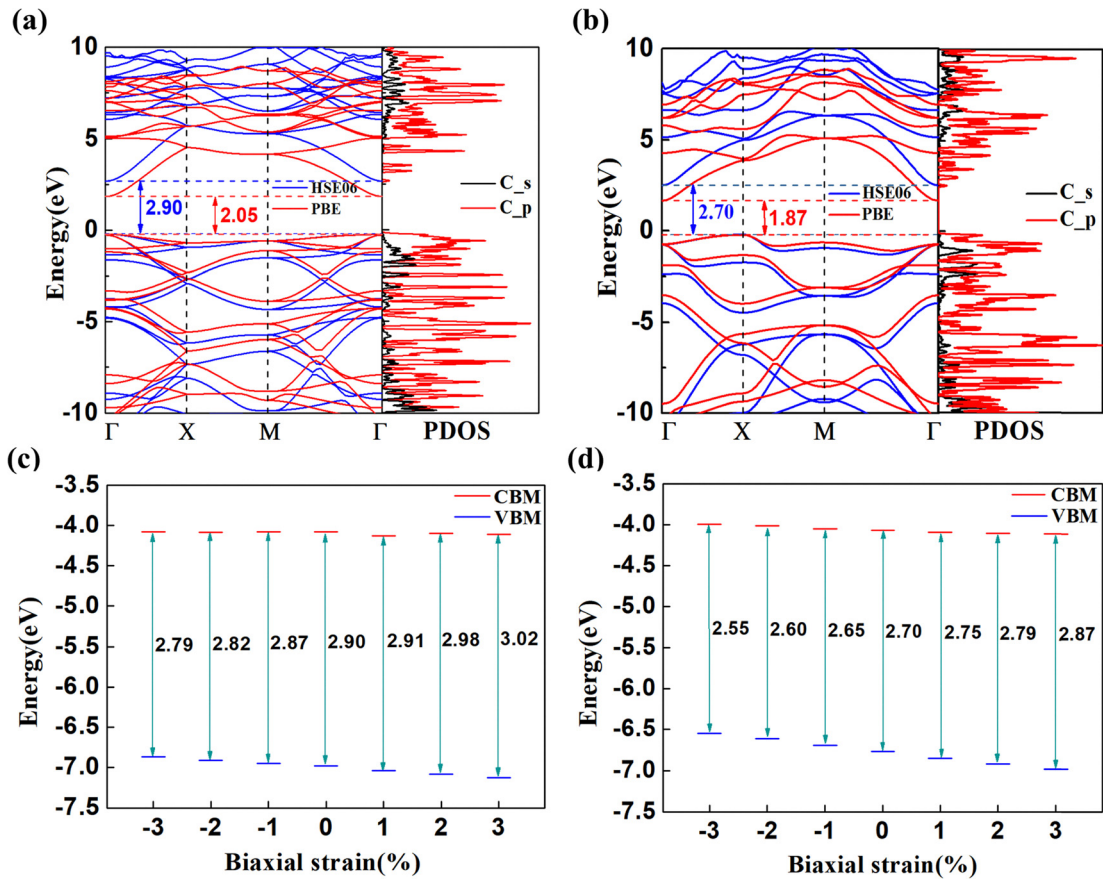

Fig. 5 Electronic band structures at the PBE/HSE06 levels and partial density of states (PDOS) involving the carbon s and p orbitals at the HSE06 level for the (a) **C_5-A** and (b) **C_5-B** monolayers. Energetic edge positions of the VBM and the CBM under biaxial strain from −3% to 3% obtained at the HSE06 level for (c) **C_5-A** and (d) **C_5-B**, respectively.

 This journal is © the Owner Societies 2025

Published on 18 Adooleessa 2025. Downloaded on 16/10/2025 3:00:56 PM.

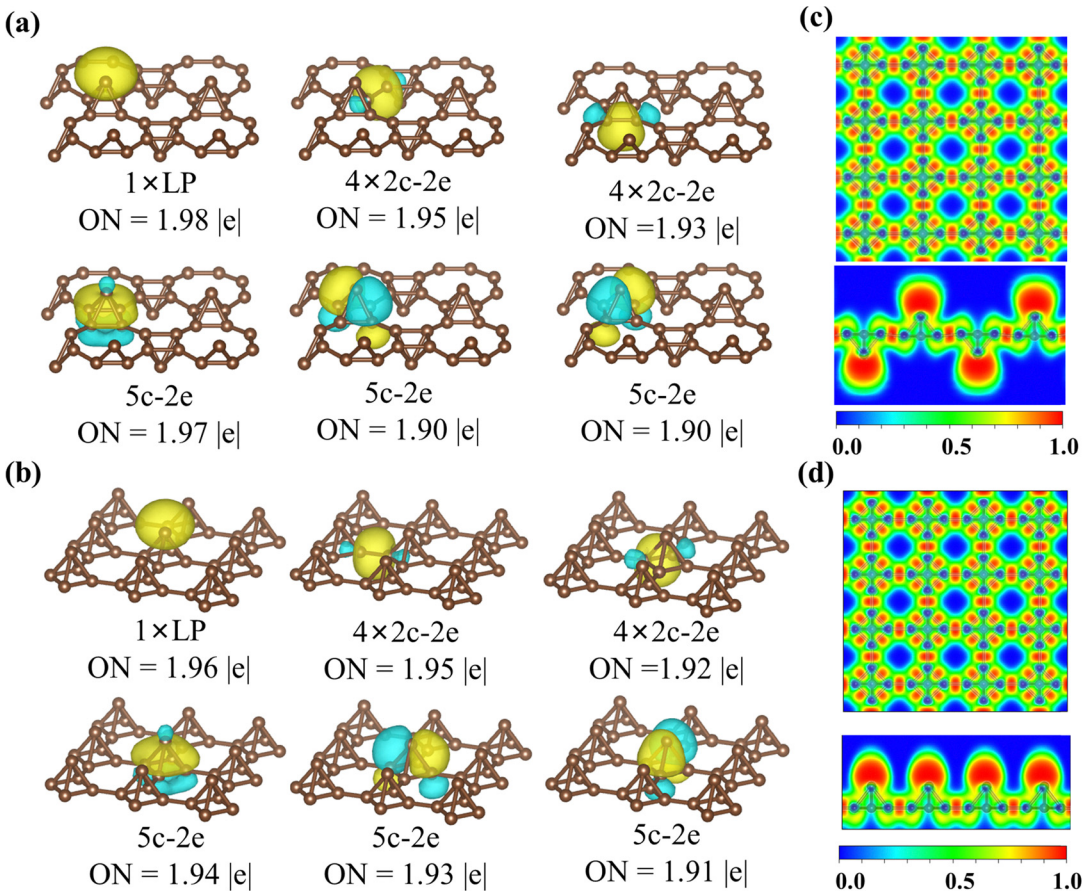

Fig. 6 SSAdNDP chemical bonding patterns for the (a) **C_5-A** and (b) **C_5-B** monolayers. Top and side views of the ELF maps for (c) **C_5-A** and (d) **C_5-B**, respectively. The blue and red colors denote the lowest (0.0) and highest (1.0) ELF values, respectively. The golden balls represent C atoms.

each apical C atom harbors an *s*-type LP, corresponding to a 1c–2e bond with an ON of 1.98 |e|. The basal C atoms adopt sp^2 hybridization, forming three C–C covalent bonds, corresponding to eight 2c–2e bonds with ONs of 1.95 and 1.93 |e|. Given the $2s^2 2p^2$ valence electron configuration for a C atom, the remaining four conjugated p-type electrons in each C_4 unit equate to the valence electrons of a 2D $^{\diamond}$O superatom (S^2P^2), which interact with the apical carbon to forge a CO-type superatomic triple bond, represented by three delocalized 5c–2e bonds. ELF calculations further clarify these bonding patterns (Fig. 6c and d). Typically, ELF values proximate to 0.0 (blue) and 1.0 (red) denote highly delocalized and strongly localized charge densities, respectively. Thus, red regions between basal carbons signify covalent bonding, while intermediate values (orange regions) between apical and basal carbons reflect multicenter bonding.

4. Conclusions

This work reports new insights into the bonding modes of the pyramidal C(C_4H_4) molecule by extending the super valence bond model to describe 2D superatom–atom super-bonding. Within this theoretical framework, the π-conjugated C_4H_4 base functions as a 2D $^{\diamond}$O superatom with four π-electrons, which interacts with the apical carbon, forming a superatomic triple bond with the electronic configuration that simultaneously fulfills the superatomic sextet rule for $^{\diamond}$O and the conventional octet law for C, similar to the bonding in the CO molecule. Significantly, we demonstrate that C(C_4H_4) can effectively substitute CO ligands in forming stable transition metal coordination complexes, where the metal atom engages in the feedback π bond with both the CO and C–C_4 π* orbitals. This electronic equivalency establishes C_5H_4 as a viable CO analogue in coordination chemistry. Additionally, two novel 2D all-carbon monolayers, **C_5-A** and **C_5-B**, composed of an assembly of super CO units, are successfully predicted. DFT calculations reveal their good dynamical, thermal, and mechanical stability, as well as practical experimental viability. These attributes, combined with moderate cohesive energies, position the monolayers as promising candidates for flexible electronic applications. Overall, this work not only provides new insights into the bonding within C(C_4H_4) but also establishes a general design strategy for advanced clusters and materials *via* 2D superatom–atom bonding.

Conflicts of interest

The authors declare no competing financial interests.

Published on 18 Adooleessa 2025. Downloaded on 16/10/2025 3:00:56 PM.

Data availability

The data supporting this article have been included as part of the article and its ESI.†

Acknowledgements

The authors acknowledge support from the National Natural Science Foundation of China (grant nos 22273001 and 22403001) and the Scientific research project of colleges and universities in Anhui Province (2024AH050058 and 2024AH050044). The calculations were carried out at the High-Performance Computing Centre of Anhui University.

References

1 V. Y. Lee and O. A. Gapurenko, *Chem. Commun.*, 2023, **59**, 10067–10086.
2 Q. Sun, C. Muck-Lichtenfeld, G. Kehr and G. Erker, *Nat. Rev. Chem.*, 2023, **7**, 732–746.
3 P. Coburger, F. Masero, J. Bösken, V. Mougel and H. Grützmacher, *Angew. Chem., Int. Ed.*, 2022, **134**, e202211749.
4 V. Y. Lee, O. A. Gapurenko, Y. Ito, T. Meguro, H. Sugasawa, A. Sekiguchi, R. M. Minyaev, V. I. Minkin, R. H. Herber and H. Gornitzka, *Organometallics*, 2016, **35**, 346–356.
5 V. Y. Lee, Y. Ito, A. Sekiguchi, H. Gornitzka, O. A. Gapurenko, V. I. Minkin and R. M. Minyaev, *J. Am. Chem. Soc.*, 2013, **135**, 8794–8797.
6 V. I. Minkin, R. M. Minyaev and R. Hoffmann, *Russ. Chem. Rev.*, 2002, **71**, 869–892.
7 S. Satpati, T. Roy, S. Giri, A. Anoop, V. S. Thimmakondu and S. Ghosal, *Atoms*, 2023, **11**, 96.
8 L. Vidal, D. Barrena-Espés, J. Echeverría, J. Munárriz and Á. M. Pendás, *ChemPhysChem*, 2024, **25**, e202400329.
9 E. Lewars, *J. Mol. Struct.: THEOCHEM*, 1998, **423**, 173–188.
10 V. I. Minkin, R. M. Minyaev and G. V. Orlova, *J. Mol. Struct.: THEOCHEM*, 1984, **110**, 241–253.
11 M. Brack, *Rev. Mod. Phys.*, 1993, **65**, 677.
12 L. Cheng, Y. Yuan, X. Zhang and J. Yang, *Angew. Chem.*, 2013, **52**, 9035–9039.
13 Z. Luo and S. Lin, *Coord. Chem. Rev.*, 2024, **500**, 215505.
14 W. Chen, W. Tian, Z. Li, J. Wang, A. Muñoz-Castro, G. Frenking and Z. Sun, *Nat. Synth.*, 2025, **4**, 471–478.
15 S. Takano and T. Tsukuda, *J. Am. Chem. Soc.*, 2021, **143**, 1683–1698.
16 H. Liu, B. Huang, Y. Shao and Y. Pei, *Small*, 2024, **20**, 2403520.
17 Y. H. Xu, X. Yang, Y. N. Yang, L. Zhao, G. Frenking and Z. M. Sun, *Nat. Chem.*, 2025, **17**, 556–563.
18 D. Li, J. Yang and L. Cheng, *Natl. Sci. Rev.*, 2022, **10**, nwac216.
19 D. Li, Z. Gui, M. Ling, L. Guo, Z. Wang, Q. Yuan and L. Cheng, *Nanoscale*, 2024, **16**, 17433–17441.
20 D. Li, C. Yan, Q. Yuan, L. Shi and L. Cheng, *Phys. Chem. Chem. Phys.*, 2023, **25**, 8439–8445.
21 M. Ling, Y. Zheng, X. Yu, Q. Yuan, L. Dan and L. Cheng, *J. Phys. Chem. Lett.*, 2025, **16**, 870–875.
22 X. Yu, P. Wu, Q. Yuan, C. Yan, D. Li and L. Cheng, *J. Phys. Chem. A*, 2023, **127**, 7487–7495.
23 L. Guo, D. Zhang, K. Shen, Q. Yuan, D. Li and L. Cheng, *J. Phys. Chem. Lett.*, 2024, **15**, 5754–5760.
24 L. Cheng, X. Zhang, B. Jin and J. Yang, *Nanoscale*, 2014, **6**, 12440–12444.
25 Z. Gui, Z. Wang, L. Guo, D. Li, Q. Yuan and L. Cheng, *J. Phys. Chem. A*, 2024, **128**, 10579–10586.
26 M. Frisch, G. Trucks, H. Schlegel, G. Scuseria, M. Robb, J. Cheeseman, G. Scalmani, V. Barone, G. Petersson and H. Nakatsuji, Wallingford, CT, 2016.
27 J. P. Perdew, M. Ernzerhof and K. Burke, *J. Chem. Phys.*, 1996, **105**, 9982–9985.
28 T. H. Dunning Jr, *J. Chem. Phys.*, 1989, **90**, 1007–1023.
29 J. P. Perdew, *Phys. Rev. B: Condens. Matter Mater. Phys.*, 1986, **33**, 8822.
30 J. P. Perdew, *Phys. Rev. B: Condens. Matter Mater. Phys.*, 1986, **34**, 7406.
31 F. Weigend and R. Ahlrichs, *Phys. Chem. Chem. Phys.*, 2005, **7**, 3297–3305.
32 D. Y. Zubarev and A. I. Boldyrev, *Phys. Chem. Chem. Phys.*, 2008, **10**, 5207–5217.
33 B. Silvi and A. Savin, *Nature*, 1994, **371**, 683–686.
34 T. Lu and F. Chen, *J. Comput. Chem.*, 2011, **33**, 580–592.
35 W. Humphrey, A. Dalke and K. Schulten, *J. Mol. Graph.*, 1996, **14**, 33–38.
36 G. Kresse and J. Hafner, *Phys. Rev. B: Condens. Matter Mater. Phys.*, 1993, **47**, 558.
37 G. Kresse and J. Hafner, *Phys. Rev. B: Condens. Matter Mater. Phys.*, 1994, **49**, 14251.
38 G. Kresse and J. Furthmüller, *Comput. Mater. Sci.*, 1996, **6**, 15–50.
39 G. Kresse and J. Furthmuller, *Phys. Rev. B: Condens. Matter Mater. Phys.*, 1996, **54**, 11169.
40 G. Kresse and D. Joubert, *Phys. Rev. B: Condens. Matter Mater. Phys.*, 1999, **59**, 1758.
41 J. P. Perdew, K. Burke and M. Ernzerhof, *Phys. Rev. Lett.*, 1996, **77**, 3865.
42 J. Paier, R. Hirschl, M. Marsman and G. Kresse, *J. Chem. Phys.*, 2005, 122.
43 H. J. Monkhorst and J. D. Pack, *Phys. Rev. B: Solid State*, 1976, **13**, 5188.
44 J. Heyd and G. E. Scuseria, *J. Chem. Phys.*, 2003, **118**, 8207–8215.
45 S. Baroni, S. De Gironcoli, A. Dal Corso and P. Giannozzi, *Rev. Mod. Phys.*, 2001, **73**, 515.
46 A. Togo and I. Tanaka, *Scr. Mater.*, 2015, **108**, 1–5.
47 G. J. Martyna, M. L. Klein and M. Tuckerman, *J. Chem. Phys.*, 1992, **97**, 2635–2643.
48 T. R. Galeev, B. D. Dunnington, J. R. Schmidt and A. I. Boldyrev, *Phys. Chem. Chem. Phys.*, 2013, **15**, 5022–5029.
49 K. Momma and F. Izumi, *J. Appl. Crystallogr.*, 2011, **44**, 1272–1276.

 This journal is © the Owner Societies 2025

50 J. Zhang, X. Liu, G. Neri and N. Pinna, *Adv. Mater.*, 2015, **28**, 795–813.
51 S. Ma, H. Zhang, Z. Cheng, X. Xie, X. Zhang, G. Liu and G. Chen, *Appl. Surf. Sci.*, 2023, **639**, 158083.
52 J. Wang, S. Yip, S. R. Phillpot and D. Wolf, *Phys. Rev. Lett.*, 1993, **71**, 4182.
53 E. Cadelano, P. L. Palla, S. Giordano and L. Colombo, *Phys. Rev. B: Condens. Matter Mater. Phys.*, 2010, **82**, 235414.
54 Z. Yin, H. Li, L. Jiang, Y. Shi, Y. Sun, G. Lu, Q. Zhang, X. Chen and H. Zhang, *ACS Nano*, 2011, **6**, 74–80.
55 S. Wang, Y. Yao, Z. Peng, B. Zhang and S. Chen, *Nanotechnology*, 2021, **32**, 415705.
56 S. Zhang, J. Zhou, Q. Wang, X. Chen, Y. Kawazoe and P. Jena, *Proc. Natl. Acad. Sci. U. S. A.*, 2015, **112**, 2372–2377.
57 J. Zhang, R. Wang, X. Zhu, A. Pan, C. Han, X. Li, D. Zhao, C. Ma, W. Wang, H. Su and C. Niu, *Nat. Commun.*, 2017, **8**, 683.

Published on 18 Adooleessa 2025. Downloaded on 16/10/2025 3:00:56 PM.